

# Journal of Biomedical Optics

BiomedicalOptics.SPIEDigitalLibrary.org

## Confocal multispot microscope for fast and deep imaging in semicleared tissues

Marie-Pierre Adam  
Marie Caroline Müllenbroich  
Antonino Paolo Di Giovanna  
Domenico Alfieri  
Ludovico Silvestri  
Leonardo Sacconi  
Francesco Saverio Pavone

**SPIE.**

Marie-Pierre Adam, Marie Caroline Müllenbroich, Antonino Paolo Di Giovanna, Domenico Alfieri, Ludovico Silvestri, Leonardo Sacconi, Francesco Saverio Pavone, "Confocal multispot microscope for fast and deep imaging in semicleared tissues," *J. Biomed. Opt.* **23**(2), 020503 (2018), doi: 10.1117/1.JBO.23.2.020503.

# Confocal multispot microscope for fast and deep imaging in semicleared tissues

Marie-Pierre Adam,<sup>a,\*†</sup> Marie Caroline Müllenbroich,<sup>a,b,†</sup> Antonino Paolo Di Giovanna,<sup>a</sup> Domenico Alfieri,<sup>c</sup> Ludovico Silvestri,<sup>a,b</sup> Leonardo Sacconi,<sup>a,b</sup> and Francesco Saverio Pavone<sup>a,b,d</sup>

<sup>a</sup>University of Florence, European Laboratory for Non-linear Spectroscopy, Florence, Italy

<sup>b</sup>National Institute of Optics, National Research Council, Florence, Italy

<sup>c</sup>L4T-LIGHT4TECH Srl, Sesto Fiorentino, Italy

<sup>d</sup>University of Florence, Department of Physics, Florence, Italy

**Abstract.** Although perfectly transparent specimens are imaged faster with light-sheet microscopy, less transparent samples are often imaged with two-photon microscopy leveraging its robustness to scattering; however, at the price of increased acquisition times. Clearing methods that are capable of rendering strongly scattering samples such as brain tissue perfectly transparent specimens are often complex, costly, and time intensive, even though for many applications a slightly lower level of tissue transparency is sufficient and easily achieved with simpler and faster methods. Here, we present a microscope type that has been geared toward the imaging of semicleared tissue by combining multispot two-photon excitation with rolling shutter wide-field detection to image deep and fast inside semicleared mouse brain. We present a theoretical and experimental evaluation of the point spread function and contrast as a function of shutter size. Finally, we demonstrate microscope performance in fixed brain slices by imaging dendritic spines up to 400- $\mu\text{m}$  deep. © The Authors.

Published by SPIE under a Creative Commons Attribution 3.0 Unported License. Distribution or reproduction of this work in whole or in part requires full attribution of the original publication, including its DOI. [DOI: [10.1117/1.JBO.23.2.020503](https://doi.org/10.1117/1.JBO.23.2.020503)]

Keywords: two-photon microscopy; multispot microscopy; deep tissue imaging; confocal line detection.

Paper 170671LR received Oct. 20, 2017; accepted for publication Jan. 15, 2018; published online Feb. 19, 2018.

Brain function and structure are intrinsically correlated and therefore best elucidated on an organ-wide scale in three-dimensional (3-D) at cellular resolution. Observing such large volumes, as, for example, intact mammalian brains, requires imaging techniques, which can penetrate deep into the tissue and ideally also afford fast image acquisition to gather statistically relevant datasets. Both issues, such as depth and speed, have been addressed by recent advances in tissue clearing

methodologies,<sup>1–3</sup> which are capable of rendering the brain transparent and thus provide optical access. The reduced scattering of cleared samples not only allows for deeper tissue imaging but also enables wide-field detection schemes that suffer from scatter-induced optical cross talk. Light-sheet microscopy (LSM),<sup>4,5</sup> a method taking advantage of wide-field detection to allow for fast acquisition speeds at cellular resolution, requires the sample to be perfectly transparent and consequently, a variety of samples that can be studied with LSM strongly depends on the effectiveness of the tissue clearing method. The most successful methodologies to render a brain transparent are also the most complex, costly, and time-consuming ones, whereas simpler and cheaper methods are now emerging, which render the brain not perfectly clear but instead “semitransparent.”

Two-photon microscopy (TPM), on the other hand, is a well-established technique<sup>6</sup> for imaging even in highly scattering media<sup>7</sup> owing to decreased scattering at long wavelengths and the signal’s quadratic dependence on the excitation intensity. Being a point-scanning technique, however, TPM suffers from slow scan rates. To increase imaging speed, several strategies have been explored, for example, multispot multiphoton microscopy (MMM) using either single spot detectors arrays<sup>8</sup> or wide-field sensors.<sup>9</sup> An increase in the speed gained by multiplexing the excitation; however, comes with a penalty in optical cross talk, which prohibits the application of MMM deep within scattering samples. In this regard, confocal line detection has been successfully employed in various microscopy techniques to eliminate out-of-focus fluorescence and reduce optical cross talk.<sup>10–12</sup>

Here, we present a mixed microscope, which aims to capitalize on the advantages of MMM while preserving the optical sectioning capabilities of confocal systems. We combined fast and robust multispot two-photon fluorescence excitation with wide-field confocal line detection to reject cross talk. Our method benefits from the increased penetration depth of two-photon excitation in scattering media and the increased imaging rates of multiplexed excitation while exploiting the rolling shutter of a fast sCMOS camera. We present a full theoretical and experimental evaluation of the microscope performance and further validate our method by imaging fine neuronal structures 400- $\mu\text{m}$  deep inside partially cleared mouse brain.

The microscope was built using a commercial inverted microscope (DMLFSA, Leica) with few modifications to the excitation and detection path [Fig. 1(a)]. Two-photon excitation was achieved with a high-power-pulsed Ti:Sa laser (Chameleon Ultra II, Coherent, 150-fs pulse width, 80-MHz repetition rate). The power at the back aperture of the microscope objective was kept below 740 mW. A line of 15 equidistant laser spots was generated at the focal plane of the microscope objective using a diffractive optic element (DOE, MS-454-920-Y-A, Holo/or). The DOE was reimaged onto the first of a pair of galvanometric mirrors (G1222HS-C355, Galvoline) using a 4f-system of unity magnification, and the second galvo was placed into a common conjugate plane using two spherical mirrors again of unity magnification. A second telescope in a 4f configuration reimaged both galvos and the DOE through the entry port of the inverted microscope onto the back aperture of the microscope objective (Zeiss, LD LCI Plan-Apochromat 25 $\times$ /0.8 Imm Corr).

In the sample, the line of excitation spots was scanned rapidly along its axis to generate a homogeneous excitation line, which in turn was scanned perpendicularly to obtain a

\*Address all correspondence to: Marie-Pierre Adam, E-mail: [marie-pierre.adam@pasteur.fr](mailto:marie-pierre.adam@pasteur.fr)

†These authors contributed equally to this work

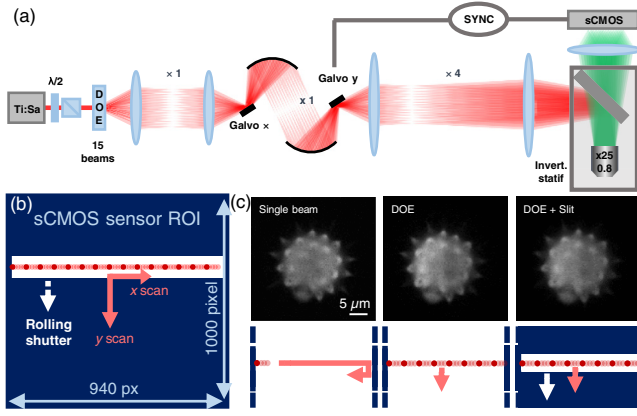


**Fig. 1** (a) Schematic of the microscope setup, (b) scheme of the rolling shutter as a synchronized confocal slit on the sCMOS camera sensor, and (c) fluorescent pollen grain for three different microscope configurations. From left to right: a single beam is scanned, 15 beams are scanned, 15 beams are scanned with a synchronized 10 pixels slit.

sheet of excitation of  $90 \mu\text{m} \times 96 \mu\text{m}$ . This field of view (FOV) resulted from the full DOE diffraction angle (5.27 deg) and total effective magnification. Fluorescence was collected in epidetection and separated from the excitation light by a long-pass dichroic mirror (FF665-Di02-25, Semrock) and bandpass filters (FF01-520/35-25 and FF01-680/SP-25, Semrock). A tube lens (450 mm) formed the primary image onto the chip of a fast sCMOS camera (PCO.edge 5.5, PCO) such that 1 pixel corresponded to 96 nm in the object plane. By sweeping the excitation line synchronously to the line readout of the camera [Fig. 1(b)], a virtual confocal slit, adjustable in height and speed, partially rejected out-of-focus fluorescence and reduced cross talk induced by tissue scattering.

3-D stacks were acquired by scanning the microscope objective along the optical axis. A custom-written LabWindows code [National Instrument (NI)] in conjunction with a data acquisition card (PCI-6221, NI) controlled and synchronized the microscope. To demonstrate illumination homogeneity, as well as shutter synchronization, the same pollen grain was imaged in three different configurations: conventional single beam scanning and multipot scanning with and without rolling shutter [Fig. 1(c)]. The slight inhomogeneity in fluorescent signal, from left to right, that can be observed in the middle and right image, is due to an inhomogeneity in diffraction efficiency of our DOE that we estimated around 0.8 between the first and last diffraction orders.

To evaluate the optical performances of the microscope, we model the image formation process similarly to what has been done for light-sheet microscopy with confocal slit detection.<sup>13</sup> We define  $x$  as the axis parallel to slit direction, and  $z$  as the optical axis of the microscope. We neglect all aberrations. We consider the intensity at  $(x, y, z)$  of light emitted from a point object at  $(0, 0, 0)$  illuminated by a single excitation spot centered at  $(x', y', z')$ . Assuming that the laser focus and camera are perfectly conjugated and synchronized, the camera sensor lies at  $z = z'$ , and the slit aperture is centered at  $y'$ . At a specific position of the scanning beam, since we are imaging on a pixelated array detector, the partial point spread function (PSF) of the microscope is simply the product of the PSF of a wide-field imaging system, denoted as  $H_{WF}$ , the laser intensity  $I_{laser}$ , and the aperture function of the slit AF

$$d^2 H_{TOT}(x, y, z, x', y', z' = z) = H_{WF}(x, y, z) \cdot I_{laser}^2(x', y', z) \cdot AF(y, y') dx' dy', \quad (1)$$

with

$$H_{WF} = \left| \int_0^1 J_0 \left( NA k_0 \rho \sqrt{x^2 + y^2} \right) \cdot e^{i \frac{k_0}{2n} NA^2 \rho^2 z} \rho d\rho \right|^2$$

$$I_{laser} = \left[ \frac{\omega_0}{\omega(z')} \right]^2 \cdot e^{-2 \left[ \frac{x'}{\omega(z')} \right]^2} \cdot e^{-2 \left[ \frac{y'}{\omega(z')} \right]^2},$$

$$AF(y, y') = \begin{cases} 1 & \text{if } |y - y'| \leq s/2 \\ 0 & \text{elsewhere} \end{cases},$$

where  $J_0$  is the zero order of the Bessel function, NA is the numerical aperture,  $k_0$  is the wave vector modulus in vacuum,  $n$  is the refractive index of the medium between the object and the objective lens,  $\omega_0$  and  $\omega(z)$  are the beam radii at the positions 0 and  $z$ , respectively, and  $s$  is the size of the slit.  $\omega(z)$  can be written as  $\omega(z) = \omega_0 \sqrt{1 + \left( \frac{z}{z_R} \right)^2}$ , where  $z_R$  is the Rayleigh range.  $H_{WF}$  is given by the Airy formula for Fraunhofer diffraction at a circular aperture<sup>14</sup> and  $I_{laser}$  as the intensity of a focused Gaussian beam since we are slightly underfilling the objective back aperture.

As the laser is scanned over the FOV,  $H_{TOT}$  corresponds to the integral sum of the intensity contributions  $d^2 H_{TOT}$  of each laser position within the slit. Assuming that the camera extent along the  $x$ -axis is much larger than the slit width and the lateral extent of the partial PSF contributions, we have

$$H_{TOT}(x, y, z) = \int_{-\infty}^{+\infty} \int_{y-\frac{s}{2}}^{y+\frac{s}{2}} H_{WF}(x, y, z) \cdot I_{laser}^2(x', y', z) dx' dy', \quad (2)$$

After simplification and using the error function  $\text{erf}(x) = \frac{2}{\sqrt{\pi}} \int_0^x e^{-t^2} dt$ , we obtain a PSF  $H_{TOT}$  of

$$H_{TOT}(x, y, z) = H_{WF}(x, y, z) \cdot \frac{\pi \omega_0^4}{8 \omega(z)^2} \cdot \left\{ \text{erf} \left[ \frac{2y + s}{\omega(z)} \right] - \text{erf} \left[ \frac{2y - s}{\omega(z)} \right] \right\}. \quad (3)$$

$H_{TOT}$  was numerically computed with Mathematica (Wolfram Research), using:  $\lambda_0 = 510 \text{ nm}$ ,  $n = 1.45$ ,  $NA = 0.8$ , and  $\omega_0 = 580 \text{ nm}$ . The refractive index, corresponding to a solution of 63% of TDE in PBS, was measured with a refractometer.  $\omega_0$  was extracted by the corresponding beam waist measured at the back focal plane of the microscope objective with the knife-edge method. The full width at half maximum (FWHM) was calculated as a function of slit size from the PSF profile  $H_{TOT}$  for the three axes, respectively.

The resolution of the microscope was evaluated as a function of slit size both theoretically and experimentally in terms of its PSF and their FWHM and is summarized in Fig. 2(a). The PSF was measured experimentally by imaging fluorescent microspheres of  $0.1\text{-}\mu\text{m}$  diameter in  $z$ -stacks (200-nm step size) for five different slits (3, 6, 12, 30, and 60 pixels). The beads (505-nm to 515-nm emission wavelength, Invitrogen) were diluted in a 63% 2,2'-thiodiethanol (TDE)/distilled water gel containing 4% of agarose. Twenty PSFs were manually extracted and fitted with Gaussian curves to obtain the

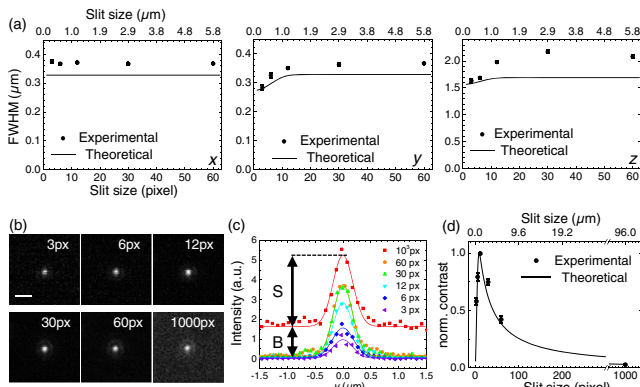


**Fig. 2** (a) FWHM of the PSF as a function of slit size in  $x$ ,  $y$ , and  $z$  ( $n = 20$  beads, errors are SD, solid line: theoretical prediction). (b) Fluorescent bead for six slit sizes. Laser power: 740 mW, line exposure time: 1.6 ms. (c)  $y$  intensity profiles and Gaussian fit of bead shown in (d). The amplitude of the Gaussian fits  $S$  and the corresponding background  $B$  was used to calculate contrast in (d). (d) Normalized contrast as a function of slit size. ( $n = 10$  beads, error is SD, solid line: theoretical prediction.)

FWHM along the 3-D [Fig. 1(a)]. The FWHMs were  $368 \pm 3$  nm in  $x$ ,  $366 \pm 3$  nm in  $y$ , and  $2.08 \pm 0.02$  μm in  $z$  for a slit size of 60 pixels [ $n = 20$ , error is standard deviation (SD)]. As the slit size decreased, the FWHMs in  $y$  and  $z$  decreased and reached  $283 \pm 9$  nm and  $1.63 \pm 0.04$  μm, respectively, for a slit of three pixels. As expected, resolution along the slit ( $x$ ) was independent of the slit size. According to theoretical calculations, with the slit fully open, the lateral and axial FWHMs are equal to 328 nm and 1.69 μm, respectively. As the slit size decreases, the FWHMs along the  $y$  and  $z$  axes decrease to 274 nm and 1.56 μm, respectively, for a slit of three pixels. The experimental values for the FWHMs are consistent with the theoretical predictions (solid lines) albeit slightly bigger, especially for larger slits ( $> 10$  pixels) probably due to spherical aberrations.

Since the rolling shutter rejects photons from out-of-focus planes, its contribution to increase image contrast was evaluated by analyzing the ratio between signal and background. The same bead was imaged successively with six slit sizes [3, 6, 12, 30, 60, and 1000 pixels, Fig. 1(b)] and its  $xy$  profile was fitted by a two-dimensional Gaussian function [Fig. 2(c)]. The images were corrected by subtracting the dark noise of the camera for each slit size. The normalized contrast, averaged over 10 beads, is shown in Fig. 2(d). With the slit corresponding to a global shutter (1000 pixels), a normalized contrast of  $0.26 \pm 0.03$  was measured. By gradually closing down the slit, more out-of-focus photons were rejected and the contrast increased up to its maximum at a slit size of 12 pixels, corresponding to approximately three PSFs. At this optimal shutter size, contrast was improved fourfold compared with the global shutter. When the slit size was further reduced, the rolling shutter not only rejected background photons but also signal photons and therefore contrast began to drop. The theoretical contrast, calculated from the normalized ratio of the theoretical signal extracted from the PSF calculation and the experimental background extracted from the bead images, was in agreement with the experimentally measured data points [Fig. 1(d), solid line].

After a comprehensive evaluation of resolution and contrast of the microscope on fluorescent beads, the imaging performance was tested on semicleared brain samples, which in

addition to increased scattering, also exhibit macroscopic mismatches in refractive index. Adult mice (Thy1-GFP<sup>M15</sup>) were prepared and their brains optically cleared according to the protocol described in Costantini et al.<sup>16</sup> With this clearing methodology, we achieved transmittances of 30% to 40% at 900 nm resulting in a refractive index compatible with our microscope objective. After overnight fixation in paraformaldehyde (PFA), brains were cut in 2-mm-thick slices and cleared by two successive incubations. The slices were put in a 20-mL PSB solution containing 30% and 63% of TDE for 1 and 3 h while rotating at room temperature.<sup>16</sup> This procedure reduces tissue scattering in samples, which were previously fixed in PFA; however, without rendering them entirely transparent. All experimental protocols were designed in accordance with Italian laws and were approved by the Italian Minister of Health (authorization no. 790/2016-PR) (Fig. 3).

Imaging performance in tissue was evaluated from  $z$  stacks of 400-μm depth (step size 2 μm) corresponding to the working distance of the microscope objective. For each depth, six images corresponding to 3, 6, 12, 30, 60, and 1000 pixels slits were successively acquired. Resolution in tissue was estimated by fitting a line profile through the neck of dendritic spines located throughout the stack [Figs. 2(a) and 2(b)] with a Gaussian curve [Fig. 2(c)] and comparing the FWHM [ $n = 11$ , error bars are standard error of the mean (SEM), Fig. 2(d)]. The reported FWHMs are slightly elevated compared with values obtained with beads due to increased scattering in the semicleared sample and spine necks not necessarily being structures under the resolution limit of the microscope. As a general trend, resolution decreased with increasing shutter size.

Image contrast was quantified at each depth by the normalized Shannon entropy of the discrete cosine transform.<sup>17</sup> For a comparative study, six regions of interest were selected over the entire FOV [Fig. 2(d)] and analyzed through depth

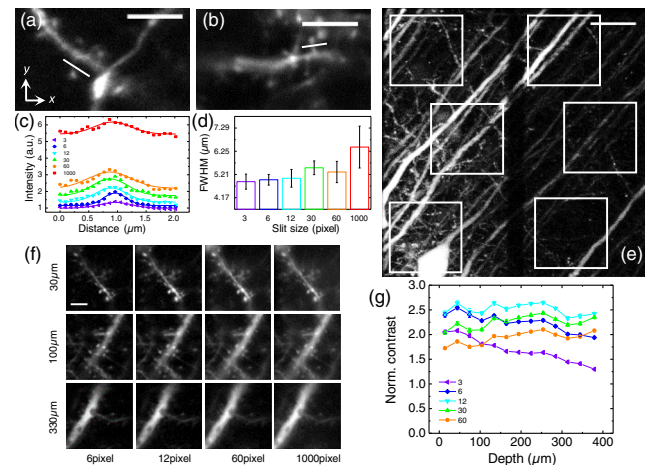


**Fig. 3** (a) and (b) Exemplary line profiles through the necks of dendritic spines. Scale bar 5 μm. (c) Intensity profiles for the line profile shown in (a) for all shutter sizes. (d) FWHM of Gaussian fits. ( $n = 11$ , error bars are SEM.) (e) Maximum intensity projection of the full FOV through the entire depth of the stack (shutter 12 pixels). Indicated are the six ROIs ( $25 \mu\text{m} \times 25 \mu\text{m}$ ) used in the contrast analysis. Scale bar 15 μm. (f) Exemplary images at different depths and different shutter sizes. Brightness has been adjusted for each image. Scale bar 5 μm. (g) Evolution of relative contrast, calculated as the normalized Shannon entropy of the discrete cosine transform with depths for all shutter sizes binned over 30 μm, and normalized by the global shutter contrast (corresponding to a slit of 1000 pixels). Error is SEM.

for all shutters. The dark stripe visible in the full FOV imaging in Fig. 2(e) is due to a suboptimal DOE, which has a lower intensity in the zero-order spot. The contrast values of the six ROIs were averaged at each depth and then binned over 30  $\mu\text{m}$ . We normalized each average contrast value by the global shutter contrast (corresponding to a slit size of 1000 pixels) and reported its evolution with depth for all shutter sizes as shown in Fig. 2(g). The general trend of increased scattering and therefore reduced contrast with increasing shutter size and increasing depth was also evident in tissue. Similar to the imaging of beads, the best contrast was achieved with a slit size of 12 pixels corresponding to three PSFs throughout the entire depths of the stack.

In summary, we have presented a mixed microscope, which operates with a robust and fast multispot two-photon excitation and a cross talk rejecting wide-field detection. The microscope was fully characterized by imaging subresolution sized fluorescent beads and semicleared mouse brains. However, we point out that the proposed method is poorly compatible with uncleared samples and *in vivo* measurements.

The frame rate of the microscope is currently limited by the galvo speed to  $\sim 100\text{-}\mu\text{s}$  per pixel line (corresponding to 10 Hz for a  $1000 \times 1000$  pixels image). A future implementation would benefit from a resonant scan system, which would shift the bottleneck to the camera line readout time (on the order of 10  $\mu\text{s}$ ), therefore corresponding to 100 Hz for a  $1000 \times 1000$  pixels image. The gain in speed scales essentially with the number of multiplexed excitation spots as long as the laser source is capable of providing the same energy per beamlet. With current Ti:Sa lasers, up to 20 beamlets of enough power (75 mW) can be generated, resulting in a 20 $\times$  increase in imaging speed. By comparison, a typical two-photon microscope with a pixel dwell time of 1  $\mu\text{s}$  achieves a frame rate of 1 Hz for the same size image. Considering that the 3-D reconstruction of large volumes such as  $2 \text{ mm} \times 6 \text{ mm} \times 0.5 \text{ mm}$  of brain tissue requires 5 days with a standard TP system, a 20 $\times$  increase in acquisition speed is highly desirable. Whereas a conventional MMM struggles with optical cross talk present in scattering tissues even at shallow depths, in the microscope presented here suppression of cross talk with a confocal rolling shutter was sufficient to distinguish dendritic spines down to a depth of 400  $\mu\text{m}$  in semicleared mouse brains.

### Disclosures

The authors have no relevant financial interests in this article and no potential conflicts of interest to disclose.

### Acknowledgments

This project received funding from the Italian Institute of Technology in Genoa and the European Union's H2020

Research and Innovation Programme under Grant Agreements No. 720270 (Human Brain Project) and 654148 (Laserlab-Europe), and from the EU programme H2020 EXCELLENT SCIENCE, European Research Council (ERC) under Grant Agreement ID No. 692943 (BrainBIT). The project has also been supported by the Italian Ministry for Education, University, and Research in the framework of the Flagship Project NanoMAX and of Eurobioimaging Italian Nodes (ESFRI Research Infrastructure), and by Ente Cassa di Risparmio di Firenze (Private Foundation).

### References

1. D. S. Richardson and J. W. Lichtman, "Clarifying tissue clearing," *Cell* **162**(2), 246–257 (2015).
2. K. Tainaka et al., "Chemical principles in tissue clearing and staining protocols for whole-body cell profiling," *Annu. Rev. Cell Dev. Biol.* **32**, 713–741 (2016).
3. L. Silvestri et al., "Clearing of fixed tissue: a review from a microscopists perspective," *J. Biomed. Opt.* **21**(8), 081205 (2016).
4. H.-U. Dodt et al., "Ultramicroscopy: three-dimensional visualization of neuronal networks in the whole mouse brain," *Nat. Methods* **4**(4), 331–336 (2007).
5. R. Tomer et al., "Advanced CLARITY for rapid and high-resolution imaging of intact tissues," *Nat. Protocol* **9**(7), 1682–1697 (2014).
6. W. Denk, J. H. Strickler, and W. W. Webb, "Two-photon laser scanning fluorescence microscopy," *Science* **248**(4951), 73–76 (1990).
7. F. Helmchen and W. Denk, "Deep tissue two-photon microscopy," *Nat. Methods* **2**(12), 932–940 (2005).
8. L. Sacconi et al., "Multiphoton multifocal microscopy exploiting a diffractive optical element," *Opt. Lett.* **28**, 1918 (2003).
9. M. Straub and S. W. Hell, "Multifocal multiphoton microscopy: a fast and efficient tool for 3D fluorescence imaging," *Bioimaging* **6**, 177–185 (1998).
10. R. Wolleschensky, B. Zimmermann, and M. Kempe, "High-speed confocal fluorescence imaging with a novel line scanning microscope," *J. Biomed. Opt.* **11**(6), 064011 (2006).
11. L. Silvestri et al., "Confocal light sheet microscopy: micron-scale neuroanatomy of the entire mouse brain," *Opt. Express* **20**(18), 20582 (2012).
12. E. Baumgart and U. Kubitschek, "Scanned light sheet microscopy with confocal slit detection," *Opt. Express* **20**(19), 21805 (2012).
13. L. Silvestri, L. Sacconi, and F. Pavone, "Correcting spherical aberrations in confocal light sheet microscopy: a theoretical study," *Microsc. Res. Tech.* **77**(7), 483–491 (2014).
14. M. Born and E. Wolf, *Principles of Optics*, 4th ed., Pergamon Press (1970).
15. G. Feng et al., "Imaging neuronal subsets in transgenic mice expressing multiple spectral variants of GFP," *Neuron* **28**(1), 41–51 (2000).
16. I. Costantini et al., "A versatile clearing agent for multi-modal brain imaging," *Sci. Rep.* **5**, 9808 (2015).
17. L. A. Royer et al., "Adaptive light-sheet microscopy for long-term, high-resolution imaging in living organisms," *Nat. Biotechnol.* **34**(12), 1267–1278 (2016).